

On the Effectiveness of Laser Speckle Contrast Imaging and Deep Neural Networks for Detecting Known and Unknown Fingerprint Presentation Attacks

Hengameh Mirzaalian¹, Mohamed Hussein^{1,2}, Wael Abd-Almageed¹

¹Information Sciences Institute, 4676 Admiralty Way #1001, Marina Del Rey, CA 90292

²Faculty of Engineering, Alexandria University, Alexandria, Egypt 21544

hengameh, mehusein, wamageed@isi.edu

Abstract

Fingerprint presentation attack detection (FPAD) is becoming an increasingly challenging problem due to the continuous advancement of attack techniques, which generate “realistic-looking” fake fingerprint presentations. Recently, laser speckle contrast imaging (LSCI) has been introduced as a new sensing modality for FPAD. LSCI has the interesting characteristic of capturing the blood flow under the skin surface. Toward studying the importance and effectiveness of LSCI for FPAD, we conduct a comprehensive study using different patch-based deep neural network architectures. Our studied architectures include 2D and 3D convolutional networks as well as a recurrent network using long short-term memory (LSTM) units. The study demonstrates that strong FPAD performance can be achieved using LSCI. We evaluate the different models over a new large dataset. The dataset consists of 3743 bona fide samples, collected from 335 unique subjects, and 218 presentation attack samples, including six different types of attacks. To examine the effect of changing the training and testing sets, we conduct a 3-fold cross validation evaluation. To examine the effect of the presence of an unseen attack, we apply a leave-one-attack out strategy. The FPAD classification results of the networks, which are separately optimized and tuned for the temporal and spatial patch-sizes, indicate that the best performance is achieved by LSTM.

1. Introduction

Biometric authentication systems are widely used since they provide a higher level of security with a lower cost. They also eliminate the need to carry identifications cards or remember complicated passwords. However, these systems are vulnerable to *presentation attacks* (PA), i.e. presentation of fake biometric samples in order to imperson-

ate an authorized user or obfuscate the identity of an illegal user. To maintain the integrity of the biometric systems, developing accurate and robust *presentation attack detection* (PAD) techniques is essential. However, due to the presence of realistic fake samples created by sophisticated attack-techniques, such as silicone and liquid latex, designing a successful PAD system is not trivial and PAD is becoming an increasingly challenging problem [21].

Fingerprint is perhaps the most conventional biometric identifier due to the long-time perception of its uniqueness, universality, measurability, and subject-friendliness [13]. Fingerprint PAD (FPAD) methods make benefit of the physiological measurement of the finger collected by the hardware-sensors [5]. These measurements are then used by a downstream algorithm (e.g. signal processing- or machine learning-based) to distinguish between bona fide (i.e. real) and PA samples. The physiological measurements provided by the sensors can be either static or dynamic. Static characteristics, such as odor [3], skin resistance [18], and measurements by infrared [27] and optical coherence tomography [8], are extracted from a single fingerprint impression. On the other hand, dynamic features are derived by processing multiple frames of the same fingerprint sample, e.g. a time series of images to measure elasticity [2, 14], heartbeat [1], blood flow [30], or multi-spectral image acquisitions of finger under different illumination conditions using different wavelengths [19]. The aforementioned approaches are commonly referred to as *hardware-based* techniques since they deploy additional hardware to the fingerprint sensing hardware. However, obviously, all such techniques involve both hardware and software components. Therefore, we may also refer to them as *hybrid* techniques. This is in contrast to *software-only* techniques, which are commonly referred to just as *software-based* techniques. Software-only techniques do not augment fingerprint sensing hardware with any additional sensors and solely depend on the data used for recognition to perform fingerprint PAD [20, 26]. The majority of the existing FPAD methods in this category apply traditional classification techniques

(e.g. support vector machine) using hand-crafted features (e.g. wavelet and graylevel co-occurrence matrix of optical images) [10, 29]. More recently, few FPAD approaches have been proposed utilizing convolutional neural networks (CNNs). Nogueira et al. [22] fine-tuned AlexNet [17] and VGG [25] architectures to preform liveness detection of the fingerprints. A classical ConvNet consisting of four 2D convolutional layers with a binary cross-entropy loss was used by Wang et al. [31] to do the FPAD task. Bhanu et al. [4] used triplet loss in their network to minimize the intra-class distances of the patches belonging to the same class while maximizing the inter-class distances. Chugh et al. [9] used MobileNet-v1 over the centered and aligned patches of the optical images to discriminate between fake and real fingerprints. Park et al. [23] included fire and gram modules within their network to learn the textures of the bona fide and PA samples. Kim et al. [16] employed deep belief networks and used contrastive divergence for FPAD.

Software-only approaches are attractive due to their low cost and applicability on the widely used legacy fingerprint sensors. However, with the increased difficulty of FPAD, it is important to explore hybrid solutions that use extra dedicated sensors for FPAD. In this regard, laser speckle contrast imaging (LSCI) has attracted very little attention in the FPAD literature despite its interesting characteristics. LSCI provides information on the flow of blood under the skin through the dynamics of speckle pattern. This information can be very valuable in discriminating between bona fide fingerprints and fake ones. Chatterjee et al. [7] conducted a study over the hardware and physics part of LSCI for FPAD and showed that there is a significant difference between the biospeckle patterns of the real fingers comparing to the patterns of the fake samples. However, the study was conducted on a very small sample and did not actually evaluate the performance of FPAD based on LSCI data. Recently, Keilbach et al. [15] performed LSCI-based FPAD by applying an SVM classifier on a set of hand crafted features, such as intensity histograms and LBP features. Later on, Hussein et al. [12] applied a simplified version of AlexNet [17] to perform LSCI-based FPAD. Both studies showed promising performance of the proposed FPAD methods using LSCI data. However, the former only relied on hand crafted features while the latter deployed a network model that did not make the best use of the temporal characteristics of the LSCI data by using only 2D convolutions. Moreover, the evaluation dataset in both works was relatively small (only 163 subjects).

In this work, we conduct a comprehensive analysis of the LSCI-based FPAD utilizing deep neural networks. Compared to the few earlier studies, our evaluation is conducted on a considerably larger dataset (335 subjects). Moreover, we explore different deep neural network architectures with the goal of making the best use of the spatial and tempo-

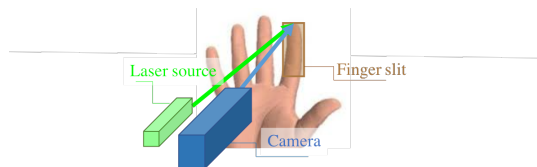
ral information in the LSCI data for FPAD. Our architectures include 2D and 3D spatial convolutional and recurrent models. We separately adapt the representation of the spatiotemporal LSCI data to the suitable format for each of the evaluated networks. All our models are patch-based, in which a classification score is estimated for each patch of the input sample, and the sample is classified based on averaging the patch-wise scores. We tune all the networks for the temporal and spatial patch-sizes. Given the optimized models, we first perform a 3-fold cross validation to examine the effect of changing the training and testing sets. Then, to examine the effect of the presence of an unseen attack, which was not included within the training phase, we apply a leave-one-attack out evaluation strategy. Cross validation results of the networks indicate that the best performance is achieved by the recurrent model and further inspection of the results indicates that the most challenging attack in our dataset is the dragon-skin overlay (Section 5).

The remainder of this paper is organized as follows. In Section 2, laser speckle contrast imaging and our capture device are briefly introduced. Section 3 discusses the proposed benchmark including details of the dataset, partitioning strategy and metrics used to evaluate various network architectures. In Section 4, we describe different deep network architectures investigated in this study. Evaluation results are presented in Section 5. Finally, conclusions are drawn in Section 6.

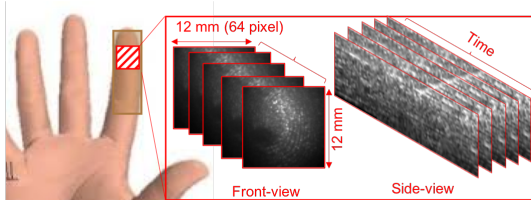
2. LSCI Capture Device

When laser light illuminates a surface, a random interference pattern will be formed by the reflected light, which is known as a speckle pattern. The speckle pattern is affected by the roughness and/or temperature of the surface. In the presence of a stationary object, the pattern is static. However, the pattern will be changed over time when there exists motion on the illuminated object, such as the movements of the blood cells under the skin surface. In fact, using laser speckle contrast imaging (LSCI), the blood perfusion of the tissue can be visualized [6]. By collecting a time-series of the LSCI data, the flow of the blood cells is detectable. Therefore, the LSCI measurements of the fingers constitute a useful liveness signal for FPAD.

Our LSCI capture device consists of a 1310 nm laser illumination source and a camera. The camera constitutes an InGaAs area sensor, which is sensitive to the 1310 nm wavelength and not sensitive to visible light. The camera is also equipped with a lens assembly. The laser beam is produced by the laser source and directed to a finger slit of dimensions $45 \text{ mm} \times 15 \text{ mm}$. A schematic diagram of the device is shown in Figure 1(a). No platen is used to cover the finger slit in our LSCI capture device. This shows that LSCI can be used in touch-less fingerprint sensors, which are generally less vulnerable to fingerprint lifting and are



(a) Schematic of our LSCI capture device



(b) Capture area and LSCI data

Figure 1. (a) A simplified illustration of the LSCI capture device, which consists of a laser source directed to the finger slit and a camera to capture the illumination reflection. (b) Area of the finger captured by the device is shown in hatched red. The middle and right images show the stacks of the 2D slices of the front-view and side-view of the LSCI data when viewed as a volume.

more desirable from the hygiene perspective [24].

For this study, the optical design is adjusted to capture a region of size $12\text{ mm} \times 12\text{ mm}$ that lies roughly in the middle of the first knuckle when the finger is placed on the slit while its tip is resting on the slit’s edge, as shown in Figure 1(b). This region was found to always contain either skin for bona fide fingers or other material for PAs. The deployed InGaAs sensor is a low resolution (64×64 pixels) and high frame rate (up to 1000 fps). In this study, the sensor is operated at a frame rate of approximately 500 fps.

3. Evaluation Benchmark

3.1. Dataset

Using the LSCI capture device explained in Section 2, we collected a large dataset of LSCI data for fingerprints. For each captured fingerprint, a sequence of 1000 frames with the laser illumination are collected and 20 frames without the laser illumination. The average of the frames captures without illumination is used for dead pixel and ambient illumination removal.

The LSCI data was collected from six fingers (the three middle fingers of each hand) of 335 unique subjects. Each subject was allowed to participate in the collection multiple times (up to three). At each participation, the subject passed by the collection station either in the absence of any attack or in the presence of up to two overlaid attacks attached to two of his/her fingers. The data was thoroughly reviewed by the research team. Samples with defects, *e.g.* due to finger motion or hardware failure, were excluded. After this process, the dataset consisted of 3743 valid bona fide and 218

Attack-type	#	Attack-type	#
Conductive paper	11	Conductive silicone	62
Transparency	26	Silicone-I	13
Silicone-II	79	Dragon-skin	27

Table 1. The number of the collected images at each of the PA categories in our dataset.

valid PA samples. The PA categories and number of collected samples per class are provided in Table 1. All used attacks are of overlay type. Two attack species have conductive coating material, one on a paper print and one on silicone. The other four attack species include two types of silicone, transparency print, and dragon-skin.

Examples of the acquired LSCI data in the presence and absence of the PAs are shown in Figure 2. As can be seen in the side-view visualization, the changes in the pixel intensity over time is more noisy in the case of bona fide samples, which is due to the more dynamic speckle pattern, which is in turn due to the blood flow.

3.2. Data Partitioning

We employ two different data partitioning strategies. In the first strategy, we use a 3-Fold partitioning to alleviate the bias resulting from a fixed division of the dataset into training, testing, and validation sets. The dataset is divided into three roughly equal sets of samples such that the data of each subject only appears in one set. Then, we create the 3-Fold partitioning by using two sets for training and one set for testing each time. 20% of the training data is separated to create a validation set such that the data of each subject either appear all in the training or the validation set in each fold. As shown in Table 2, the distribution of the bona fide and different PA samples are approximately the same among the three folds.

In order to evaluate the ability to detect previously *unknown attacks* (i.e. attacks that were present in the training data), we use a leave-one-attack-out (LOAO) data partitioning strategy. Since the dataset consists of six PA species (Section 3.1), we divide the dataset into six folds this time. The bona fide samples in the training, testing, and validation sets are fixed in all the folds. The training and validation sets of each fold include PA samples of only five of the PA species while all the samples the remaining PA species are put in the testing set. For example, the training set of Fold#0 does not have any sample belonging to the conductive paper species, where the testing set of that fold contains all the conductive paper samples. Table 3 shows the distribution of the data samples per fold of the LOAO partitioning.

3.3. Evaluation Metrics

Let P and N represent the total numbers of the attack (positive) and bona fide (negative) testing sample, respectively. Given the number of false positives, FP , and num-

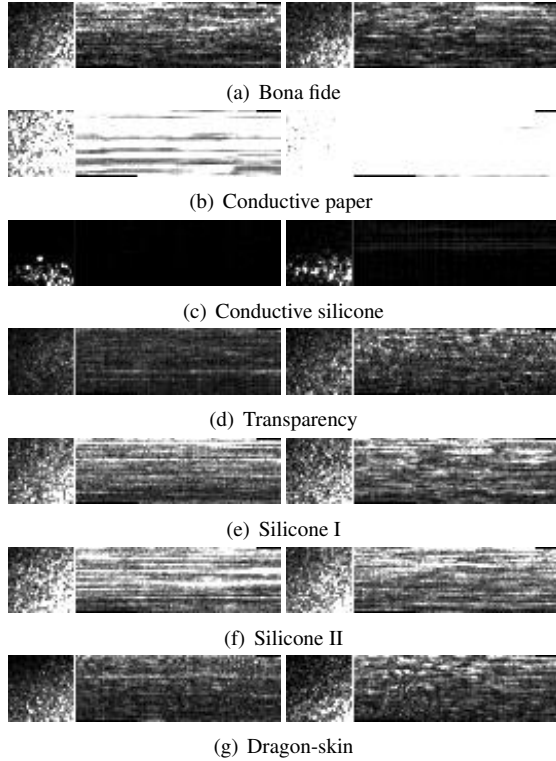


Figure 2. Sample LSCI data in the absence (a) and presence of PAs (b-g). Each subfigure represents the front-view, i.e. first frame (64×64), and side-view, i.e. frames border (64×100), of a 100-frame LSCI data when viewed as a volume, for two different subjects within each category (a-g). All pixel values in each volume are normalized to cover the display’s dynamic range for visualization purposes.

number of false negatives, FN , in the FPAD classification results of a given trained model, we measure the performance of the model in terms of the following metrics: i) bona fide presentation classification error rate $BPCER = FN/N$; ii) attack presentation classification error rate $APCER = FN/P$; iii) average classification error rate $ACER = 0.5(BPCER + APCER)$; iv) $BPCER$ at $APCER$ of 5% denoted by $BPCER_{20}$; and v) area under the Receiver Operating Characteristic (ROC) curve, AUC .

4. Patch-based FPAD Techniques for LSCI

To perform FPAD using LSCI data, we investigate several patch-based neural network architectures. Based on the way deep networks consume LSCI data, these architectures can be categorized into three main groups: i) 2D architecture; ii) 3D architecture; and iii) temporal architecture. Since we are essentially using a new sensing modality (i.e. LSCI) and obtaining large amounts of training data is not feasible, we adopt a patch-based approach, in which we feed the neural network the LSCI patches, instead of the entire LSCI image. The architectural details of each of the

studied architectures and the patch sampling technique used for training them are explained in the following sections.

4.1. Deep Neural Network Architectures

We use the architecture proposed by Hussein et al. [12] as our baseline network (BaseN). As shown in Figure 3(a), BaseN consists of six consecutive 2D convolution (Conv) layers, where each 2D Conv is connected to a ReLU module. The output of the last 2D Conv layer is passed to a fully connected layer followed by a sigmoid layer to predict the PA probability score for the given input image patch.

As depicted in Figure 3(b), the second network (ResN) is constructed by adding residual connections between every two 2D convolution layers of the BaseN. To make sure that the number of channels in the residual branch match the output of the main branch in each residual block, a 2D convolution layer is added to each residual connection.

Our third network (Figure 3(c)) contains inception modules (IncpN). The structure of this network is inspired by the GoogLeNet [28]. However, to account for the relatively limited number of LSCI data samples, we make our IncpN model as a shallower version of GoogLeNet.

To capture discriminative features along both spatial and temporal dimensions of the LSCI data, the fourth network (Conv3) is made as a 3D version of the BaseN model by using 3D convolution and pooling layers instead of the 2D ones used in BaseN. As shown in Figure 3(d), the 3D filters are of size $5 \times 3 \times 3$ and the number of the filters at each convolution layer is set similar to those of BaseN.

The last network is made of a double-layer long short-term memory (LSTM) units with a hidden state of size 100. Compared to the other networks, the input data to the LSTM units has to be 1D vectors. Therefore, the input images are vectorized in this case, as shown in Figure 4 and explained in Section 4.2.

The predicted PA probability score provided by each of the applied CNN networks (Figure 3) falls in the range $[0, 1]$, where 1 indicates that the input patch belongs to a PA region. To make a prediction for an entire input sample, the average of patch scores is used and a threshold of 0.5 is used to make the final predictions, i.e. the presence or absence of any PA within the image.

All of the studies architectures are optimized using Adam with binary cross entropy loss and a learning rate of 2×10^{-4} . They are trained within 50 epochs with a batch size of 64. The final model is set to be the one that minimizes the loss in the validation data.

4.2. Patch Generation

Having access to a large enough number of training samples is a critical issue for training deep neural networks. Given that our LSCI dataset is limited to 3957 images, sim-

Folds	Bona fide			Conductive paper			Conductive silicone			Transparency			Silicone-I			Silicone-II			Dragon-skin		
	train	test	val	train	test	val	train	test	val	train	test	val	train	test	val	train	test	val	train	test	val
Fold#0	1986	1240	517	6	3	2	34	20	8	14	9	3	42	26	11	7	4	2	14	9	4
Fold#1	1985	1254	504	6	4	1	33	21	8	14	8	4	42	27	10	7	4	2	14	9	4
Fold#2	1978	1249	516	6	4	1	33	21	8	14	9	3	42	26	11	6	5	2	14	9	4

Table 2. Distribution of the data per fold of the 3-Fold partitioning strategy (Section 3.2).

Folds	Bona fide			Conductive paper			Conductive silicone			Transparency			Silicone-I			Silicone-II			Dragon-skin		
	train	test	val	train	test	val	train	test	val	train	test	val	train	test	val	train	test	val	train	test	val
Fold#0	3476	79	188	0	11	0	58	0	4	24	0	2	75	0	4	12	0	1	25	0	2
Fold#1	3476	79	188	10	0	1	0	62	0	24	0	2	75	0	4	12	0	1	25	0	2
Fold#2	3476	79	188	10	0	1	58	0	4	0	26	0	75	0	4	12	0	1	25	0	2
Fold#3	3476	79	188	10	0	1	58	0	4	24	0	2	0	79	0	12	0	1	25	0	2
Fold#4	3476	79	188	10	0	1	58	0	4	24	0	2	75	0	4	0	13	0	25	0	2
Fold#5	3476	79	188	10	0	1	58	0	4	24	0	2	75	0	4	12	0	1	0	27	0

Table 3. Distribution of the data per fold of the LOAO partitioning strategy (Section 3.2). The red-color encoded zeros indicate the type of the PA excluded from the training-set at each fold (each row), e.g. Fold#0 (first row) does not contain any image in the presence of conductive-print PA within the training data.

ilar to the prior FPAD works [12, 4, 22], we adopt a patch-based approach in our pipeline.

Each input sample is split into a set of small patches by sliding a window over the region of interest (ROI). In our implementation, the region of interest was set to be the central 32×32 pixel region in each LSCI frame, which was found to enjoy the maximum intensity of the laser illumination in our experimental setup. The deep networks are then trained over the generated patches. Given a test sample, patches are generated in the same way, and the classification scores are computed for each. The final score of the entire test sample is set as the average score over all patches.

The generated patches are 3D tensors of size $h \times w \times t$, where $h \times w$ are the spatial patch dimensions and t is the temporal dimension of the LSCI data. The temporal dimension of the patch is interpreted as the input channels by the 2D-model networks (BaseN, ResN, IncpN in Section 4.1), whereas it is counted as the third dimension of a 3D volume by the 3D-model network (Conv3 in Section 4.1). Suppose the patch’s tensor is represented as a collection of 2D slices over time, $[\mathbb{F}_{h \times w}^1 \mathbb{F}_{h \times w}^2 \dots \mathbb{F}_{h \times w}^t]$. Feeding a patch to a 2D- or a 3D-model network is straightforward. However, for the LSTM network, a mapping function, $\Pi : \mathbb{F}_{h \times w}^i \mapsto \vec{v}^i$, has to be applied on each 2D slice of the temporal data $\mathbb{F}_{h \times w}^i$ to map it to a 1D vector. Typically, a convolutional network can be used to perform this mapping, e.g. [11]. However, in our case, due to the small input size, we adopt simple re-shaping in our system. Therefore, each 2D frame $\mathbb{F}_{h \times w}^i$ is mapped to a vector of size $hw \times 1$ denoted by $\mathbb{F}_{hw \times 1}^i$.

As shown in Figure 4, the input to the LSTM network is t vectors of size $hw \times 1$: $[\mathbb{F}_{hw \times 1}^1 \mathbb{F}_{hw \times 1}^2 \dots \mathbb{F}_{hw \times 1}^t]$. In our implementation, the output of the last hidden state is passed to the fully connected layer at the end of the network.

In Section 5, we empirically evaluate the effect of the spatial and temporal patch-sizes by testing the networks

over: $h \times w \in [8 \times 8, 16 \times 16, 32 \times 32, 64 \times 64]$ spatial-patch sizes and $t \in [5, 10, 50, 100]$ temporal-patch-sizes.

5. Experimental Evaluation

FPAD classification performance is evaluated, per fold, for each of the studied architectures (BaseN, ResN, IncpN, Conv3, and LSTM) in terms of the metrics described in Section 3.3. The mean and standard deviation (std) of the metrics are computed over the total number of the folds for each of the partitioning strategies. Each of the studied architectures has been tuned separately for the spatial and temporal patch-sizes within the following ranges: $h \times w \in [8 \times 8, 16 \times 16, 32 \times 32, 64 \times 64]$ for the spatial-patch sizes and $t \in [5, 10, 50, 100]$ for the temporal-patch-sizes.

The averaged-ROC curves and means and stds for the three-fold partitioning are shown in Figure 5(a) and Table 4, respectively. The performance of the LSTM architecture supersedes other studied architectures for FPAD, which is intuitive since the LSTM learn the inherent temporal dynamics of bona fide presentations and presentation attacks.

Similarly, ROC curves and the means and stds for the LOAO strategy are shown in Figures 5(b)-5(f) and Table 5, respectively. Overall, it can be seen that the LSTM again outperforms other architectures. By inspecting the results of the different folds of the LOAO strategy at Figures 5(b)-5(f), it can be seen that the most challenging fold, which has the worse performance by each of the networks, is Fold#5 corresponding to the dragon-skin attack.

Table 6 shows the effect of varying patch-sizes for the LSTM network, which has the best FPAD performance. The results indicate that the performances are reduced by increasing the spatial-patch-size from 8×8 to 16×16 . Our justification for this behavior is that increasing the spatial-patch-size leads to an increase to the number of the weights

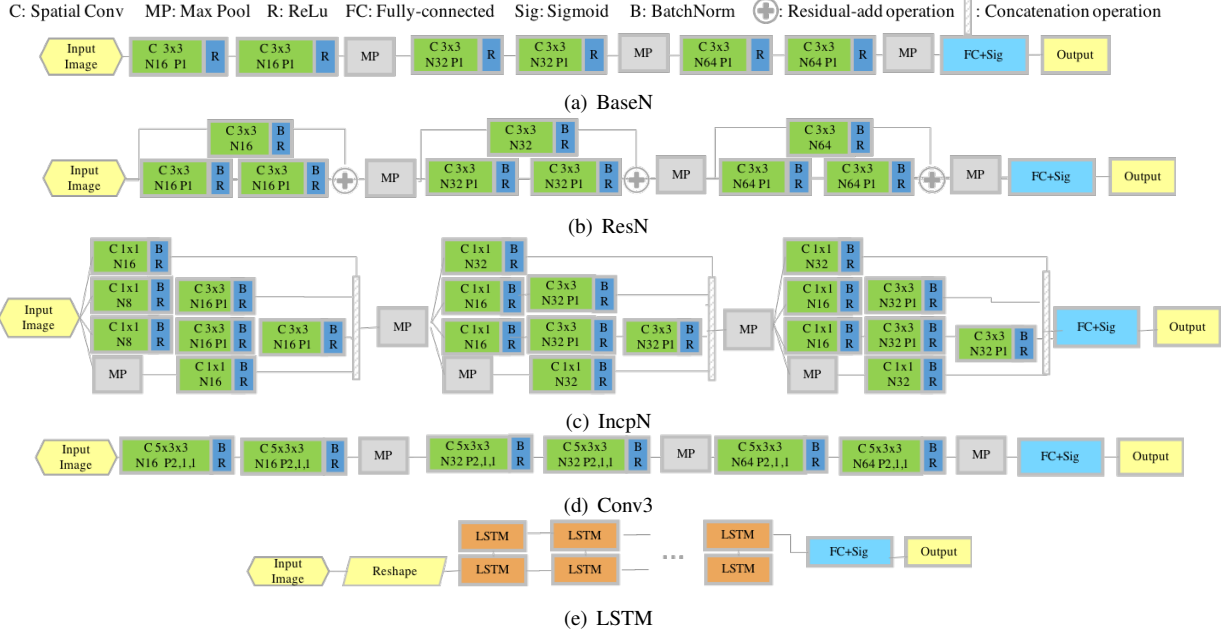


Figure 3. Different network structures applied to perform FPAD over LSCI data (Section 4.1). Depending on the way these models are incorporating the temporal dimension of the LSCI data to the network, they can be categorized to: i) 2D-model (BaseN, ResN, IncpN); ii) 3D-model (Conv3); and iii) Temporal-model (LSTM). The parameters of the convolutional layer are provided in front of the C, N, and P characters, e.g. C 3x3: kernel-size of 3x3, N16: out-channel size of 16; and P1: padding of size 1 and the default padding-size is 0.

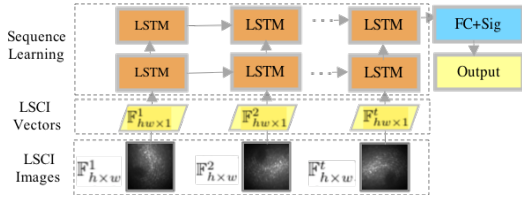


Figure 4. LSCI-LSTM network fed by a sequence of the vectorized images of the LSCI-2D frames.

to be trained by the network, which needs having access to a larger training-dataset. On the other hand, given a fixed spatial-patch size ($h \times w$), it can be seen that expanding the temporal patch-size (t) improves the performance, possibly because the LSTM has access to more temporal samples considering this fact that within the LSTM network the weights are shared across time.

6. Conclusions

Towards deeper analysis of the LSCI modality and its effectiveness, we collected a dataset consisting of 3961 LSCI images (3743 bona fide and 218 PA cases), including six different attack-types (conductive paper, conductive silicone, transparency, silicone-I, silicone-II, and dragon-skin), collected from 335 unique subjects. We applied a variety of deep neural network architectures, including spatial 2D and 3D convolutions, and a combination of both using LSTM

modules. All the networks were tuned for the spatial and temporal patch-sizes. We performed our validations following a 3-Fold partitioning strategy. Moreover, we deployed a leave-one-attack-out strategy due to the importance of assessing the ability to detect an unseen attacks. Validation results indicates that the best FPAD classification performance was achieved by LSTM network. Further inspection of the results shows that dragon-skin overlays constitute the most challenging attack in our dataset. Investigating the reasons behind the difficulty of dragon skin attacks for LSCI is certainly part of our future work. We are planning on collecting more data with much more PA sample counts and variety. Furthermore, we consider the fusion among different models and other modalities towards reaching higher FPAD performance, particularly, for unseen attacks.

Acknowledgment

This research is based upon work supported by the Office of the Director of National Intelligence (ODNI), Intelligence Advanced Research Projects Activity (IARPA), via IARPA R&D Contract No. 2017-17020200005. The views and conclusions contained herein are those of the authors and should not be interpreted as necessarily representing the official policies or endorsements, either expressed or implied, of the ODNI, IARPA, or the U.S. Government. The U.S. Government is authorized to reproduce and distribute reprints for Governmental purposes notwithstanding

	APCER	BPCER	ACER	BPCER20	TPR02	TPR0	AUC
BaseN	0.125±0.070	0.008±0.008	0.066±0.031	0.032±0.027	0.872±0.056	0.839±0.065	0.989±0.008
ResN	0.091±0.039	0.033±0.038	0.062±0.027	0.067±0.060	0.823±0.089	0.754±0.092	0.989±0.010
IncpN	0.098±0.080	0.103±0.124	0.100±0.050	0.057±0.046	0.808±0.060	0.739±0.104	0.985±0.012
Conv3	0.134±0.055	0.005±0.006	0.069±0.026	0.023±0.008	0.839±0.057	0.816±0.072	0.991±0.006
LSTM	0.097±0.042	0.006±0.005	0.052±0.020	0.019±0.015	0.881±0.041	0.858±0.049	0.992±0.006

Table 4. PAD classification results of the BaseN, ResN, IncpN, Conv3, and LSTM networks. Results are reported in terms of APCER, BPCER, ACER, BPCER20, TPR02 and AUC metrics at different columns. The reported values are in percentages and reflect the average and std of the metric computed over the 3-folds of the 3-Fold partitioning (Section 3.2).

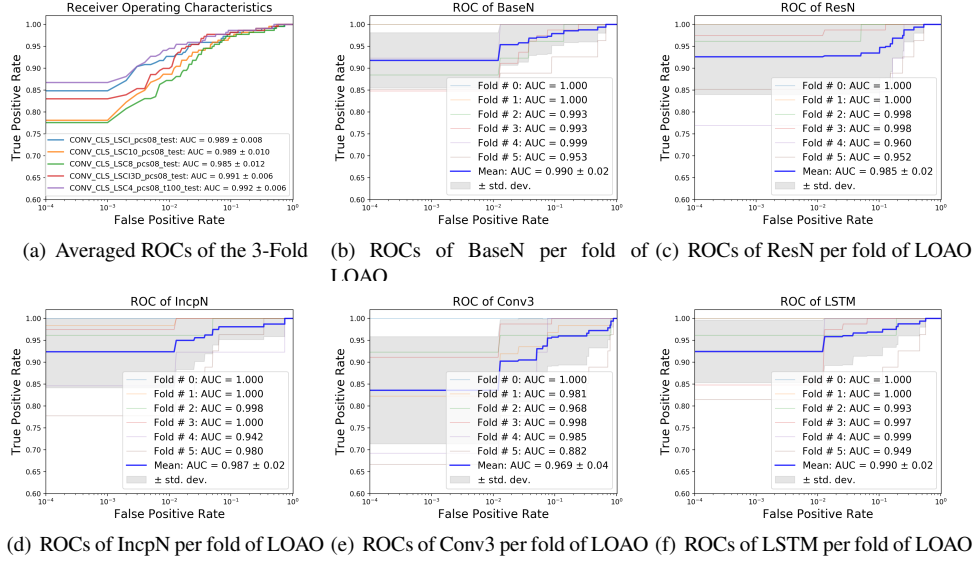


Figure 5. ROC curves of the different partitioning. (a) Averaged ROC curves of the networks based on the 3-Fold partitioning. (b-f) ROC curves of the networks per-fold of the LOAO partitioning and averaged ROCs.

any copyright annotation thereon.

References

- [1] A. Abhyankar and S. Schuckers. Integrating a wavelet based perspiration liveness check with fingerprint recognition. *Pattern Recognition*, 42(3):452–464, 2009.
- [2] A. Antonelli, R. Cappelli, D. Maio, and D. Maltoni. Fake finger detection by skin distortion analysis. *IEEE Information Forensics and Security*, 1(3):360–373, 2006.
- [3] D. Baldisserra, A. Franco, D. Maio, and D. Maltoni. Fake fingerprint detection by odor analysis. In *International Conference on Advances in Biometrics*, pages 265–272, Berlin, Heidelberg, 2006. Springer-Verlag.
- [4] B. Bhanu and A. Kumar. Deep learning for biometrics. *Advances in Computer Vision and Pattern Recognition*, 2017.
- [5] E. Bowden-Peters, R. C. W. Phan, J. N. Whitley, and D. J. Parish. *Fooling a Liveness-Detecting Capacitive Fingerprint Scanner*, pages 484–490. Springer Berlin Heidelberg, 2012.
- [6] D. Briers, D. D. Duncan, E. Hirst, S. Kirkpatrick, M. Larsson, W. Steenbergen, T. Stromberg, and O. Thompson. Laser speckle contrast imaging: Theoretical and practical limitations. *Journal of biomedical optics*, 18:66018, 06 2013.
- [7] A. Chatterjee, V. Bhatia, and S. Prakash. Anti-spoof touchless 3d fingerprint recognition system using single shot fringe projection and biospeckle analysis. *Optics and Lasers in Engineering*, 95(C):1–7, 2017.
- [8] Y. Cheng and K. V. Larin. Artificial fingerprint recognition by using optical coherence tomography with autocorrelation analysis. *Appl. Opt.*, 45(36):9238–9245, Dec 2006.
- [9] T. Chugh, K. Cao, and A. K. Jain. Fingerprint spoof buster. *CoRR*, abs/1712.04489, 2017.
- [10] R. Derakhshani, S. Schuckers, L. Hornak, and L. O. Gorman. Neural network-based approach for detection of liveness in fingerprint scanners. *Pattern Recognition*, 36(2):383–396, 2003.
- [11] J. Donahue, L. A. Hendricks, S. Guadarrama, M. Rohrbach, S. Venugopalan, K. Saenko, and T. Darrell. Long-term recurrent convolutional networks for visual recognition and description. In *CVPR*, 2015.
- [12] M. E. Hussein, L. Spinoulas, F. Xiong, and W. Abd-Elmageed. Fingerprint presentation attack detection using a novel multi-spectral capture device and patch-based convolutional neural networks. *WIFS*, pages 1–8, 2018.
- [13] A. K. Jain, K. Nandakumar, and A. Ross. 50 years of biometric research: Accomplishments, challenges, and opportunities. *Pattern Recognition Letters*, 79:80–105, 2016.

	APCER	BPCER	ACER	BPCER20	TPR02	AUC
BaseN	0.139±0.121	0.002±0.005	0.070±0.059	0.097±0.178	0.918±0.063	0.990±0.017
ResN	0.220±0.330	0.000±0.000	0.110±0.165	0.103±0.150	0.926±0.086	0.985±0.020
IncpN	0.226±0.240	0.000±0.000	0.113±0.120	0.135±0.275	0.924±0.082	0.987±0.021
Conv3	0.165±0.155	0.013±0.007	0.089±0.074	0.160±0.281	0.836±0.122	0.969±0.040
LSTM	0.092±0.093	0.000±0.000	0.046±0.047	0.080±0.168	0.925±0.071	0.990±0.018

Table 5. PAD classification results of the BaseN, ResN, IncpN, Conv3, and LSTM networks. Results are reported in terms of APCER, BPCER, ACER, BPCER20, TPR02 and AUC metrics at different columns. The reported values are in percentages and reflect the average and std of the metrics computed over the 6-folds of the LOAO partitioning (Section 3.2).

$h \times w \times t$	APCER	BPCER	ACER	BPCER20	TPR02	AUC
4x4x5	0.239±0.176	0.000±0.000	0.119±0.088	0.175±0.240	0.897±0.094	0.981±0.026
4x4x10	0.286±0.286	0.000±0.000	0.143±0.143	0.116±0.159	0.918±0.076	0.985±0.022
4x4x50	0.194±0.152	0.000±0.000	0.097±0.076	0.072±0.133	0.941±0.070	0.990±0.018
4x4x100	0.143±0.127	0.000±0.000	0.071±0.063	0.084±0.120	0.935±0.069	0.990±0.015
8x8x5	0.194±0.160	0.000±0.000	0.097±0.080	0.105±0.186	0.846±0.134	0.987±0.018
8x8x10	0.192±0.160	0.000±0.000	0.096±0.080	0.091±0.175	0.860±0.130	0.988±0.018
8x8x50	0.160±0.117	0.000±0.000	0.080±0.059	0.093±0.185	0.912±0.071	0.988±0.020
8x8x100	0.092±0.093	0.000±0.000	0.046±0.047	0.080±0.168	0.925±0.071	0.990±0.018
16x16x5	0.212±0.303	0.008±0.006	0.110±0.149	0.080±0.135	0.837±0.160	0.989±0.017
16x16x10	0.214±0.299	0.006±0.006	0.110±0.147	0.072±0.133	0.876±0.144	0.989±0.018
16x16x50	0.162±0.195	0.011±0.009	0.087±0.094	0.137±0.279	0.836±0.167	0.985±0.027
16x16x100	0.169±0.193	0.006±0.006	0.088±0.095	0.167±0.334	0.878±0.104	0.982±0.035
32x32x5	0.235±0.171	0.002±0.005	0.119±0.084	0.078±0.109	0.842±0.145	0.989±0.013
32x32x10	0.191±0.156	0.002±0.005	0.097±0.077	0.044±0.067	0.873±0.128	0.994±0.010
32x32x50	0.148±0.125	0.000±0.000	0.074±0.063	0.116±0.188	0.907±0.099	0.987±0.024
32x32x100	0.220±0.188	0.000±0.000	0.110±0.094	0.053±0.087	0.885±0.136	0.993±0.013

Table 6. Impact of varying patch-sizes $h \times w \times t$ (first column) on the classification results of the LSTM network for the LOAO partitioning. The values represent the mean and std of the metrics computed over the 6-folds of the LOO partitioning (Section 3.2).

- [14] J. Jia, L. Cai, K. Zhang, and D. Chen. A new approach to fake finger detection based on skin elasticity analysis. In *International Conference on Advances in Biometrics*, pages 309–318, Berlin, Heidelberg, 2007. Springer-Verlag.
- [15] P. Keilbach, J. Kolberg, M. Gomez-Barrero, C. Busch, and H. Langweg. Fingerprint presentation attack detection using laser speckle contrast imaging. In *2018 International Conference of the Biometrics Special Interest Group (BIOSIG)*, pages 1–6, Sep. 2018.
- [16] S. Kim, B. Park, B. S. Song, and S. Yang. Deep belief network based statistical feature learning for fingerprint liveness detection. *Pattern Recognition Letters*, 77:58 – 65, 2016.
- [17] A. Krizhevsky, I. Sutskever, and G. E. Hinton. Imagenet classification with deep convolutional neural networks. In F. Pereira, C. J. C. Burges, L. Bottou, and K. Q. Weinberger, editors, *Advances in Neural Information Processing Systems* 25, pages 1097–1105. Curran Associates, Inc., 2012.
- [18] S. S. Kulkarni and H. Y. Patil. Survey on fingerprint spoofing, detection techniques and databases. *International Journal of Computer Applications*, 95(C):30–33, 2017.
- [19] D. Maltoni, D. Maio, A. K. Jain, and S. Prabhakar. *Handbook of Fingerprint Recognition*. Springer Publishing Company Incorporated, 2nd edition, 2009.
- [20] E. Marasco and A. Ross. A survey on antispoofing schemes for fingerprint recognition systems. *ACM Comput. Surv.*, 47(2):28:1–28:36, Nov. 2014.
- [21] S. Marcel, M. S. Nixon, and S. Z. Li. *Handbook of Biometric Anti-Spoofing: Presentation Attack Detection*. Springer International Publishing, 2018.
- [22] R. Nogueira, R. de Alencar Lotufo, and R. Machado. Fingerprint liveness detection using convolutional neural networks. *IEEE Trans. Inf. Forensics Secur.*, 11(6):1206–1213.
- [23] E. Park, X. Cui, W. Kim, and H. Kim. End-to-end fingerprints liveness detection using convolutional networks with gram module. 03 2018.
- [24] G. Parziale. *Touchless Fingerprinting Technology*, pages 25–48. Springer London, 2008.
- [25] K. Simonyan and A. Zisserman. Very deep convolutional networks for large-scale image recognition. *CoRR*, 1409, 2014.
- [26] C. Sousedik and C. Busch. Presentation attack detection methods for fingerprint recognition systems: a survey. *IET Biometrics*, 3(4):219–233, 2014.
- [27] H. Steiner, S. Sporrer, A. Kolb, and N. Jung. Design of an active multispectral SWIR camera system for skin detection and face verification. *Journal of Sensors*, 2016:16–17, 2016.
- [28] C. Szegedy, W. Liu, Y. Jia, P. Sermanet, S. Reed, D. Anguelov, D. Erhan, V. Vanhoucke, and A. Rabinovich. Going deeper with convolutions. In *Computer Vision and Pattern Recognition (CVPR)*, 2015.
- [29] B. Tan and S. Schuckers. Liveness detection for fingerprint scanners based on the statistics of wavelet signal process-

ing. In *Computer Vision and Pattern Recognition Workshop*, pages 26–26, June 2006.

- [30] P. G. Vaz, A. Humeau-Heurtier, E. Figueiras, C. Correia, and J. Cardoso. Laser speckle imaging to monitor microvascular blood flow: A review. *IEEE Reviews in Biomedical Engineering*, 9:106–120, 2016.
- [31] C. Wang, K. Li, Z. Wu, and Q. Zhao. A DCNN based fingerprint liveness detection algorithm with voting strategy. *Chinese Conference on Biometric Recognition*, 35:241–249, 2015.